Investigations of radiation pressure : optical side-band cooling of a trampoline resonator and the effect of superconductivity on the Casimir force

Eerkens, H.J.

6

Details of the Experimental Techniques

In the past, measurements of the Casimir force were performed using different kinds of experimental set-ups. The first measurements relied on macroscopic objects, such as two metallic parallel plates [44] or a lens and a plate [45, 46]. Technological progress allowed an enhanced force sensitivity and sensor read-out, as well as force measurements between microscopic surfaces. Modern set-ups for Casimir force measurements include torsion pendulums [47, 50], atomic force microscopes [51, 52, 54, 142–144], microelectromechanical systems [145], micromechanical cantilevers [135] and micromechanical torsional oscillators [11, 146, 147]. For an overview of Casimir force experiments, see for example Refs. [98, 148].

In this thesis we will use a set-up based on atomic force microscopy. We have attached a polystyrene sphere with $200\,\mu$m diameter on a micromechanical cantilever, such that the cantilever and sphere act as a force sensor [149]. When the sphere is positioned above a plate, any force between the sphere and plate causes changes in the cantilever motion. We read out this motion using fiber interferometry [92, 150]. The first part of this chapter will describe fiber interferometry in more detail and its possibilities and limits when applied to our set-up. We also investigate the use of graded index (GRIN) lenses to focus the light onto the cantilever.

Since surface roughness influences Casimir force measurements, it is important that the surfaces can still be considered flat at the smallest sphere-plate separation. We will show topography images of our gold coated sphere as well as of the two plate coatings that are used for Casimir force measurements in this thesis: gold and the superconductor niobium titanium nitride. We will also show that cooling has no effect on the gold coating of the sphere.

A description of our measurement method will follow in chapter 7. There we will explain that it depends on the potential we set on the plate. We simultaneously want to perform a conductance measurement of the superconducting plate to check whether it is in its normal or superconducting state. These two measurements may not interfere. In the final part of this chapter we will explain our plate resistance detection scheme that can run simultaneously with our Casimir force measurement.

6.1 Fiber interferometry

Fiber interferometry [92, 150] is based on the interference between light reflected at the end facet of a single-mode fiber and light that is reflected at a surface some distance d in front of the fiber end facet. Since the light originates from the same laser source and follows the same path through the fiber, the interference signal is in principle only sensitive to changes between the fiber end and reflective surface. In order to deduce a general formula for the interferometer signal, we need to know the amplitudes of the two reflected beams, which are indicated in Figure 6.1.

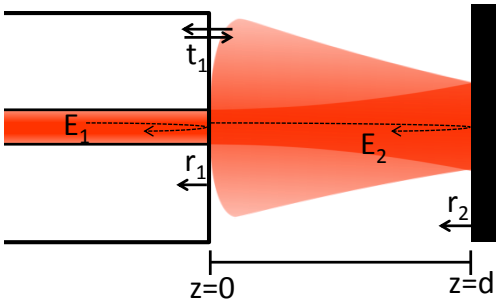

Figure 6.1: Schematic image of a fiber end in front of a reflective surface, separated by a distance d. Also shown are the reflection and transmission coefficients and the paths of the two interfering beams with amplitudes E_1 and E_2.

Light propagates through the fiber and encounters a 4% intensity reflection at the fiber-to-air interface. The normalized amplitude of the Gaussian beam reflected at this surface is given by [151]:

$$E_1(r,t) = -r_1\sqrt{\frac{2}{\pi}}\frac{1}{w_0}e^{-\frac{r^2}{w_0^2}}e^{-\mathrm{i}\omega t}, \tag{6.1}$$

where $r^2 = x^2 + y^2$, $-r_1$ is the reflection coefficient at the fiber-to-air interface[1], w_0 is the beam waist at $z = 0$ and ω is the angular frequency of the light.

The second beam is coupled out of the fiber, reflected at the second surface a distance d away and coupled back into the fiber. In the first step, the amplitude is multiplied by the transmission coefficient t_1. The light then travels a distance z where the beam waist w and radius of curvature R are altered according to:

$$w(z) = w_0\sqrt{1 + \left(\frac{z}{z_R}\right)^2} \tag{6.2}$$

$$R(z) = z + \frac{z_R^2}{z} \tag{6.3}$$

[1]Note the minus sign, which is due to time-reversal invariance. The Stokes relations dictate a phase difference of $180°$ between internally and externally reflected light [152].

with the Rayleigh length $z_R = \pi w_0^2/\lambda$ and λ the wavelength of the light. At the second surface, the light picks up a reflection coefficient r_2. The light then travels back to the fiber end facet; the total travel distance is equal to $2d$. Since both the beam waist and radius of curvature have changed, the beam no longer overlaps with the fiber core. We need to find the coupling coefficient that describes how much light couples back into the fiber. The effect of the radius of curvature can be ignored, however, regardless of the travel distance. For small distances, the curvature hasn't changed much and the beam is still effectively flat. At large distances the beam is curved significantly, but since the beam has expanded as well, we can assume that the beam is locally flat at the fiber core[3]. So we just look at the coupling coefficient between a beam with waist $w(z)$ and the fiber mode with waist w_0. Since the beams are normalized, the coupling coefficient is given by the overlap integral:

$$\begin{aligned}\eta_c(z) &= \int_0^\infty \frac{2}{\pi}\frac{1}{w_0} e^{-\frac{r^2}{w_0^2}} \frac{1}{w(z)} e^{-\frac{r^2}{w^2(z)}} 2\pi r \,\mathrm{d}r \\ &= \frac{2w_0 w(z)}{w_0^2 + w^2(z)} = \frac{2\sqrt{1+(z/z_R)^2}}{2+(z/z_R)^2}. \end{aligned} \tag{6.4}$$

Considering this coupling coefficient and an extra factor t_1 to account for the transmission back into the fiber, the amplitude of the second beam in the fiber is given by

$$E_2(r, t+\tau) = \eta_c t_1^2 r_2 \sqrt{\frac{2}{\pi}} \frac{1}{w_0} e^{-\frac{r^2}{w_0^2}} e^{-\mathrm{i}\omega(t+\tau)}, \tag{6.5}$$

where $\tau = 2d/c$ is the time delay resulting from the extra path length. The detector signal W follows from the autocorrelation function of the sum of the two beams [153], multiplied by the detector responsivity ρ:

$$W(d,f) = \rho\langle\{E_1(r,t) + E_2(r,t+\tau)\}^*\{E_1(r,t) + E_2(r,t+\tau)\}\rangle \tag{6.6}$$

$$\begin{aligned} &= \frac{\rho}{T}\int_{-T/2}^{T/2} \{E_1(r,t) + E_2(r,t+\tau)\}^*\{E_1(r,t) + E_2(r,t+\tau)\}\mathrm{d}t \\ &= \rho\left[r_1^2 \frac{2}{\pi w_0^2} e^{-\frac{2r^2}{w_0^2}} + \eta_c^2 t_1^4 r_2^2 \frac{2}{\pi w_0^2} e^{-\frac{2r^2}{w_0^2}} - \eta_c r_1 t_1^2 r_2 \frac{2}{\pi w_0^2} e^{-\frac{2r^2}{w_0^2}} (e^{-\mathrm{i}\omega\tau} + e^{\mathrm{i}\omega\tau})\right] \\ &= \rho I_1 + \rho I_2 - 2\rho\sqrt{I_1 I_2}\cos(\omega\tau). \end{aligned} \tag{6.7}$$

The first (second) term can be recognized as the intensity of the first (second) beam, while the last term is the interference term. In this term one can recognize the interferometric visibility

$$V(d) = \frac{2\sqrt{I_1 I_2}}{(I_1 + I_2)} = \frac{2\eta_c(d) r_1 t_1^2 r_2}{(r_1^2 + \eta_c^2(d) t_1^4 r_2^2)}. \tag{6.8}$$

[3]Mathematically, the condition holds if we can ignore the contribution $\mathrm{e}^{\frac{\mathrm{i}\pi r^2}{\lambda R(z)}}$ of the radius of curvature to the Gaussian beam, which is true if $\frac{\pi r^2}{\lambda R(z)} < 1$. At the fiber core, $r = w_0$, so the condition becomes $\frac{\pi w_0^2}{\lambda} = z_R < z + \frac{z_R^2}{z} = R(z)$, which always holds.

If we call $W_0 = \rho(I_1 + I_2)$ the midpoint signal, we can rewrite the previous equation in a more compact form

$$W(d, f) = W_0 - W_0 V \cos\left(\frac{4\pi f d}{c}\right). \tag{6.9}$$

A fiber interferometer is often used to detect small fluctuations ($\Delta d \ll \lambda$) on top of a large gap distance ($d \gg \lambda$). The sensitivity to detect these fluctuations is maximum at the quadrature point, which can be achieved by either tuning the gap distance or the laser frequency. In our set-up, we fix the gap distance and tune the laser frequency to quadrature. Since the visibility decreases at large distance, this gap distance cannot be too large. But if the gap distance is small, the frequency scan range of the laser can be insufficient to find the quadrature point. To overcome the requirement to operate the interferometer at quadrature point, the signal can be modulated. The modulated term in the interference signal is at phase quadrature with the original term, therefore always warranting maximal sensitivity. Since distance modulation is often not feasible, commercial interferometers tend to modulate the laser frequency, which may result in added noise to the signal. In chapter 7 we will describe this method in more detail.

The gap distance in the interferometer that reads out the cantilever motion is fixed at $200 - 300\,\mu$m, which is small enough to obtain a high visibility and large enough for our laser to scan almost half a period of the cosine in the interferometer signal. We therefore do not use any modulation techniques in this read-out.

The interferometers are fed by a $1550\,$nm, $20\,$mW laser module with a frequency scan range of $250\,$GHz. We use two distributed feedback (DWDM DFB) lasers with adjacent frequency ranges (Thorlabs LS5-C-24A-20-NM and LS5-C-22A-20-NM) to increase the scan range even further. The laser module where the frequency is in quadrature point is used for the cantilever interferometer, the other is used to read out the motion of the plate under the cantilever. The light of each laser first passes through an optical isolator (Thorlabs IO-H-1550APC) to protect the laser from back-reflected light. The light then goes through a 90/10 fiber coupler (Thorlabs 10202A-90-APC) of which the 90% port is terminated and the 10% port is connected to a fiber with a cleaved fiber end. The reflected light passes the coupler again, now 90% falls onto a detector (Thorlabs PDA10CS).

With the cantilever interferometer we want to detect small forces that are manifested as small deviations in the cantilever motion. A question that arises is what the smallest detectable motion, or noise floor, is. The noise floor is mostly influenced by mechanical noise from vibrations from the outside world. But even when the set-up is mechanically stable, there is an intrinsic noise floor caused by the laser phase noise. This noise floor can be calculated from the laser linewidth using the interferometer signal. We want to know the influence of the laser linewidth Δf on the signal linewidth ΔW when the laser is tuned at quadrature ($\sin(4\pi f d/c) = 1$):

$$\Delta W = W_0 V \frac{4\pi d}{c} \sin\left(\frac{4\pi f d}{c}\right) \Delta f = W_0 V \frac{4\pi d}{c} \Delta f. \tag{6.10}$$

To obtain the signal noise floor in meters, we divide the signal linewidth by the

sensitivity $4\pi W_0 V/\lambda$ and the square root of the bandwidth B:

$$\Delta d_{\min} = \frac{d\lambda}{c}\frac{\Delta f}{\sqrt{\mathrm{B}}}. \tag{6.11}$$

With a fiber-to-cantilever distance $d = 200\,\mu$m, laser wavelength $\lambda = 1550\,$nm and linewidth $\Delta f < 10\,$MHz we find a noise floor of $\Delta d_{\min} < 327\,\mathrm{fm}/\sqrt{\mathrm{Hz}}$ for a bandwidth of $1\,$kHz. To check this value, we measured the spectrum of the cantilever interferometer signal, shown in Figure 6.2. The cantilever motion is clearly visible around $2.3\,$kHz. From a fit through the data, we could obtain a resonance frequency of $2306\,$Hz and mechanical quality factor $Q = 4.85\times10^3$. These are reasonable values for a cantilever in vacuum at room temperature. This tells us that the fit is reasonable, despite the fact that the spectrum analyzer's low frequency noise has not been taken into account in the fit. From the fit we determine a noise floor of $103\,\mathrm{fm}/\sqrt{\mathrm{Hz}}$. This is somewhat lower than the calculated value, but differences can be explained by a smaller fiber-to-cantilever distance and lower laser linewidth.

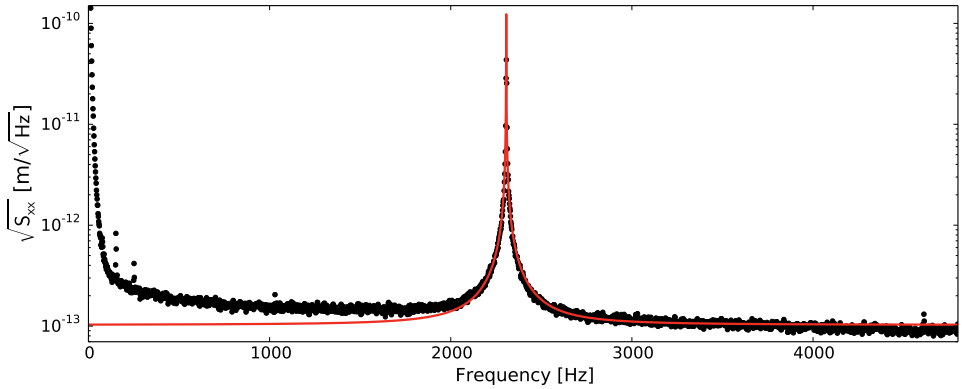

Figure 6.2: Noise spectrum from the cantilever interferometer signal. The cantilever motion at $2.3\,$kHz is clearly visible. From a fit (red line) through the data we could determine a noise floor of $103\,\mathrm{fm}/\sqrt{\mathrm{Hz}}$. This value is somewhat lower than the calculated value of $327\,\mathrm{fm}/\sqrt{\mathrm{Hz}}$, which may be explained by a lower laser linewidth or smaller fiber-to-cantilever distance. The low frequency range of the spectrum is dominated by pink noise from our spectrum analyzer, which is not taken into account in the fit.

We have compared our home build fiber interferometer with several commercially available interferometers from Optics11 (OP1550) and Attocube (IDS3010). The OP1550 came in two versions, standard with a sampled grating distributed Bragg reflector (SG-DBR) laser diode or upgraded with an external-cavity diode laser (ECL). The interferometers of Optics11 could be directly connected to our set-up, such that the measurements could be obtained under similar circumstances. The Attocube interferometers can only be combined with their sensor heads, that require a large distance between the reflective surfaces of at least several millimeters. All interferometers showed a higher noise floor. The noise floor of the OP1550 was $3\,\mathrm{pm}/\sqrt{\mathrm{Hz}}$

for the SG-DBR laser and $300\,\mathrm{fm}/\sqrt{\mathrm{Hz}}$ for the ECL. With the IDS3010 we measured a noise floor between 22 and $33\,\mathrm{pm}/\sqrt{\mathrm{Hz}}$ depending on the sensor head. This shows that the flexible use of commercial interferometers limits their achievable sensitivity and that our noise floor of $100\,\mathrm{fm}/\sqrt{\mathrm{Hz}}$ is very reasonable. It is especially advantageous that our interferometer can operate at very small distances, since the noise floor depends linearly on the fiber-to-cantilever distance when the dominant noise source is laser phase noise. Note that this requires a laser with a reasonably large frequency scan range, such that the laser can always be set at the quadrature point.

When the distance can no longer be decreased, the noise floor can be lowered by using a laser with a smaller linewidth. But this effect is not limitless. Interference occurs between all reflected light beams, not just between light reflected at the fiber end facet and at the cantilever. Reflections at for example fiber connectors may result in unwanted interferences. Due to small changes in the fiber length caused by temperature fluctuations in the cryostat, or changes in the amount of the light reflected at the connectors, the unwanted interferences do not just add a static background. All vibrations in the system now show up in the interferometer signal. Since interference can only occur between coherent beams, a solution to avoid this effect is to lower the coherence length of the laser to the fiber-to-cantilever distance. This however also enlarges the laser linewidth, so a compromise has to be made. Our lasers allow for coherence control via a small signal modulation on the laser current. The effect of this modulation is depicted in the noise spectrum of our cantilever interferometer signal in Figure 6.3. The laser current was modulated at $18.5\,\mathrm{kHz}$ at different modulation depths. The laser linewidth can be increased from less than $10\,\mathrm{MHz}$ with no modulation to more than $1\,\mathrm{GHz}$ at full modulation. The red line in Figure 6.3 displays the noise spectrum without any modulation, which results in

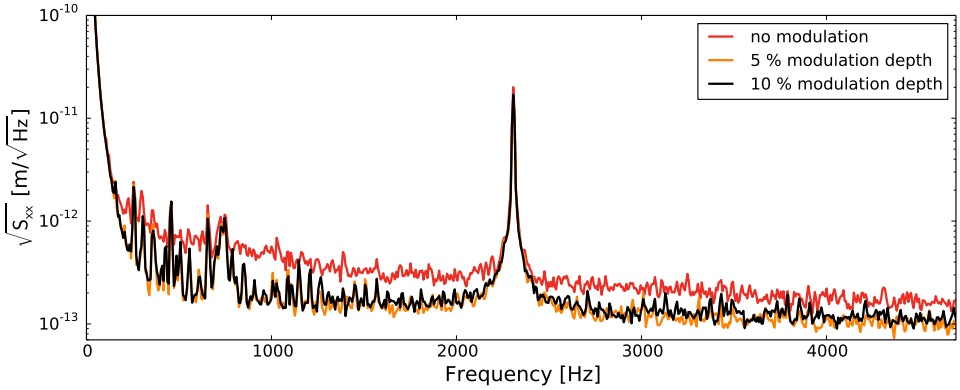

Figure 6.3: Noise spectrum from the cantilever interferometer, without modulation (red line) and with 5 percent (orange line) and 10 percent (black line) modulation. The modulation decreases the noise floor by a factor of three, but a modulation depth of more than a few percent has no further effect. The noise peaks are caused by noise in our electronics and by mechanical vibrations in our cryostat.

a noise floor of about $300\,\mathrm{fm}/\sqrt{\mathrm{Hz}}$. A modulation depth of five percent lowers the noise floor roughly three times, but further reduction of the coherence length has no more influence on the noise floor. We therefore kept the modulation at a modulation depth of five percent during our measurements.

6.1.1 GRIN lenses to focus light

Our measurement scheme based on interferometric read-out of the cantilever motion assumes only interference between the light reflected at the fiber end facet and cantilever. Spurious reflections will result in parasitic interferences in our signal. Especially harmful is light reflected at the plate underneath the cantilever, because that results in a parasitic interference that changes during a measurement run while the cantilever-plate distance is varied. To prevent this, several options are available. Decreasing the laser coherence length to only several hundred micrometers is technically not achievable. The plate can be made from an absorptive material, but this will severely limit the choice of materials for the Casimir measurements. Another option is to position the fiber under an angle, to prevent light reflected at the plate from coupling back into the fiber (compare with the read-out in atomic force microscopes via a quadrature detector), but this will also influence the read-out of the cantilever motion. The best option is to use the cantilever to block the light from the fiber before it reaches the plate. Especially since a relatively large sphere is attached to the cantilever, this proofs to be a practical solution. It is not completely reliable, however, because during our sample fabrication we have no way to check that all the light is blocked.

The possibility of stray light to couple back into the fiber is significant since the light from the fiber is divergent. We therefore investigated the option to focus the light onto the cantilever, using graded index lenses because of their size and compatibility with fibers. A graded index (GRIN) lens is a cylindrical rod where the index of refraction varies radially [152] according to

$$n(r) = n_0 \left(1 - \frac{\zeta^2 r}{2}\right), \tag{6.12}$$

where n_0 is the index of refraction at the center and ζ a positive constant indicating the variation towards the curved edge. How the light is propagated through the lens is determined by the change in refraction index and by its length. A common use of GRIN lenses is to collimate light from a fiber by placing a lens with the correct length directly behind it. The collimated light then has a beam waist (radius) of roughly 40 to $200\,\mu$m for commercial GRIN lenses. This is still too large compared to our cantilever width of $50\,\mu$m. By increasing the distance between the fiber and GRIN lens (distance v in Figure 6.4), it is possible to focus the beam onto the cantilever.

The resulting beam waist and the required distances depend on the GRIN lens and can be calculated via ray matrices [154, 155], with the ray matrix describing the propagation through a GRIN lens given by [151]

$$M_{\mathrm{GRIN}} = \begin{bmatrix} \cos(\zeta z) & \sin(\zeta z)/n_0\zeta \\ -n_0\zeta \sin(\zeta z) & \cos(\zeta z) \end{bmatrix}, \tag{6.13}$$

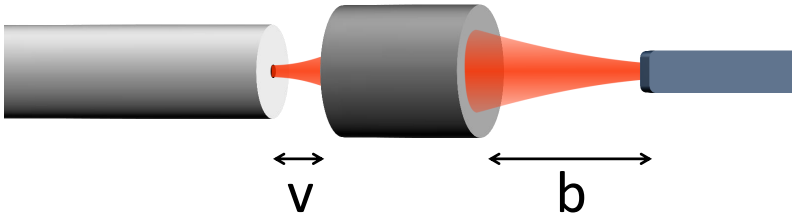

Figure 6.4: Diagram of the single mode fiber (left), graded index (GRIN) lens (middle) and cantilever (right). The light beam path is indicated, as well as the fiber-to-lens distance v and lens-to-cantilever distance b. By focusing the beam onto the cantilever via a GRIN lens, it is less likely that light reflects on the plate under the cantilever and is coupled back into the fiber to cause unwanted interference.

where z is the length of the lens. To block the light completely with the cantilever, a beam waist of less than $25\,\mu$m is required. This can be achieved with distances v and b of several millimeters. Combined with the GRIN lens length of several millimeters, this results in a distance of at least $8\,$mm between the cantilever and the fiber end facet. These are the only reflective surfaces in the set-up, since GRIN lenses are AR coated to suppress extra reflections on the facets. However, a gap of $8\,$mm significantly increases the noise floor of the interferometer, such that the cantilever motion can no longer be detected. A technically challenging solution would be to apply anti-reflection coatings on the fiber end and on one facet of the GRIN lens, such that the reflective surface is now the facet of the GRIN lens positioned closest to the cantilever. But even then the minimum gap distance is of the order of a millimeter.

Therefore, a reliable way to focus the beam onto the cantilever using GRIN lenses could not be obtained with commercially available lenses. A custom-made GRIN lens designed for a small gap between the reflective surfaces may still be a solution, but this would have to be investigated further.

6.2 Sample characterization

As a second step in our set-up characterization, we take a closer look at our samples. Our force probe is a polystyrene sphere (Thermo Scientific 4320A, radius $100\,\mu$m) that is attached to a micromechanical cantilever (Bruker RESP-20) with UV-curable adhesive (NOA 81), using a micropositioning system. The sphere and cantilever are then coated with a $4\,$nm titanium adhesion layer and a $200\,$nm conductive layer of gold in a sputtering machine (Leybold Z400).

A larger sphere radius increases the strength of the force. Also, in our data analysis we use several approximations that become more valid with larger sphere radius, as will be discussed in chapter 7. The largest commercially available spheres that we could find which still have an acceptable surface roughness [156], have a radius of $100\ \mu$m.

Surface roughness influences the strength of the Casimir and electrostatic forces at small distances and can even influence the effective separation [157, 158]. Therefore, the surface roughness limits the smallest distance at which the Casimir force can be reliably measured. Figure 6.5 shows an investigation of the large and small scale surface roughness of our spheres. The scanning electron microscope (SEM) image in Figure 6.5(a) shows that there are some flakes on the sphere. These may prevent an approach closer than several micrometers if they are located in the area of closest approach. There are, however, no other larger scale irregularities. Note that even though the SEM image is taken with a beam energy of $15\,\mathrm{kV}$, no charging effects are shown on the sphere surface. This means that the gold layer is indeed conductive.

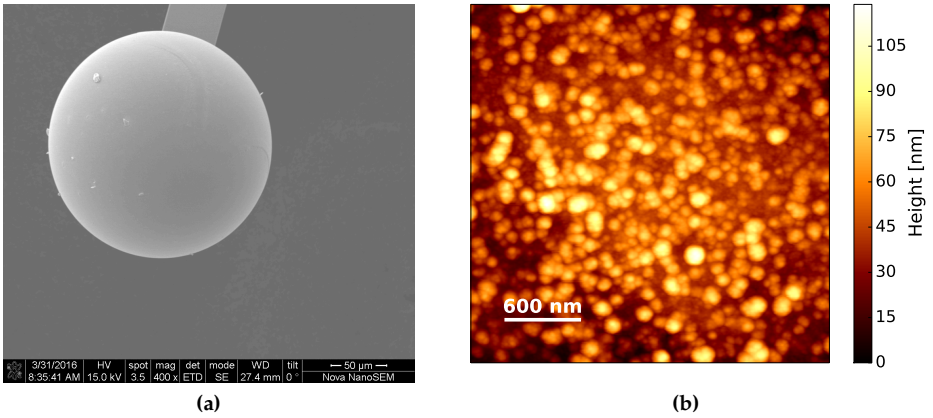

(a) (b)

Figure 6.5: Characterization of the surface roughness of our force sensor, a $100\,\mu$m radius sphere attached to a cantilever and coated with a $200\,$nm conductive layer of gold: (a) SEM image, except for some micrometer sized flakes, there is no large scale surface roughness; (b) AFM topography image ($3\,\mu$m by $3\,\mu$m) of the sphere surface, the surface roughness has an RMS value of $16.8\,$nm.

A tapping-mode atomic force microscopy (AFM) topography image of the sphere surface is shown in Figure 6.5(b). The surface roughness has an RMS value of $16.8\,$nm, mostly due to the surface roughness of the polystyrene sphere. Therefore, an approach of several tens of nanometers is in principle possible without a significant effect of surface roughness.

These force probes are meant to be operated at a base temperature of $4\,$K. But it is unknown whether the difference in thermal contraction between the polystyrene sphere and gold layer will cause the gold layer to flake. The SEM images in Figure 6.6 show the effect of cooling a gold coated sphere to $4\,$K and warming up again. There is no difference visible before (Figure 6.6(a)) and after (Figure 6.6(b)) cool-down. This means that effects like peeling do not occur and that the force probes can safely be used at low temperatures.

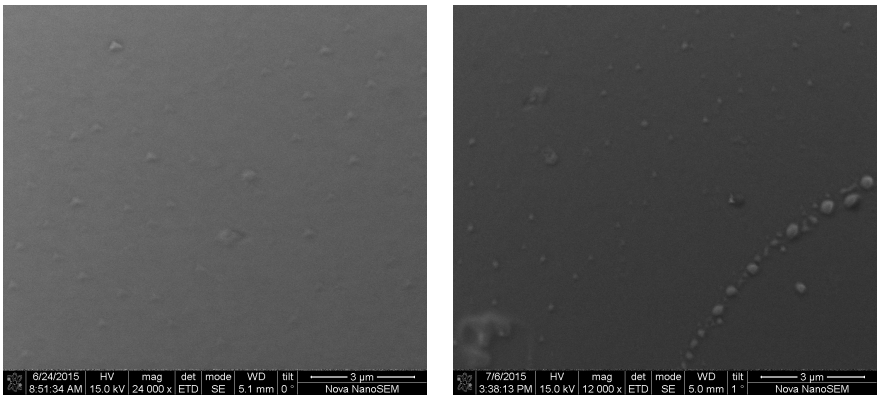

(a) **(b)**

Figure 6.6: SEM images of the gold coated sphere surface (a) before and (b) after cooling the sphere down to $4\,\mathrm{K}$. The absence of notable differences shows that cooling does not affect the coating on the spheres.

The distance of closest approach is not only determined by the surface roughness of the sphere, but also by that of the plate. The plate's surface roughness is determined with tapping-mode AFM topography scans. The scans are shown in Figure 6.7 for the different plate materials that were used: $150\,\mathrm{nm}$ gold on sapphire and $200\,\mathrm{nm}$ niobium titanium nitride (NbTiN) on SiO_2 respectively. From these scans we can determine the RMS surface roughness as $0.75\,\mathrm{nm}$ for gold and $1.13\,\mathrm{nm}$ for NbTiN. For all materials it should be possible to approach the sphere up to several tens of nanometers and we consider the plates to be perfectly flat for all practical purposes.

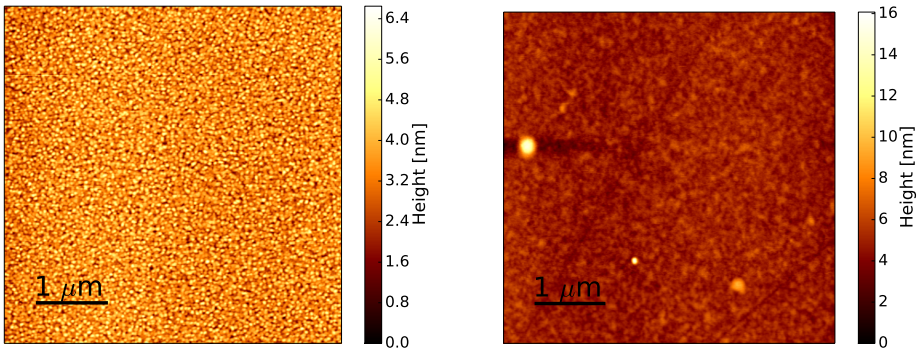

(a) **(b)**

Figure 6.7: AFM topography images of the plates used for Casimir force measurements: (a) $150\,\mathrm{nm}$ gold on sapphire, with a surface roughness of $0.75\,\mathrm{nm}$ RMS; (b) $200\,\mathrm{nm}$ NbTiN on SiO_2, with a surface roughness of $1.13\,\mathrm{nm}$ RMS

6.3 Plate resistance

Even though the NbTiN plate is made of a superconducting material, we want to be sure that the plate is superconducting at the time of a Casimir force measurement. Therefore we designed a resistance bridge that constantly compares the current through the plate with that through a reference resistance. We do not want this measurement to interfere with the Casimir measurements, where the calibration is based on the voltage $V = V_{\mathrm{DC}} + V_{\mathrm{AC}}$ between the sphere and the plate. This means we do not want our resistance detection scheme to cause any high voltages at the center of the plate, where the sphere is positioned. So we keep the potential of the plate's center at the voltage $V_{\mathrm{DC}} + V_{\mathrm{AC}}$ with respect to the sphere and then lift and lower the potential at the edges of the plate, each with a voltage $V_{\mathrm{b}}/2$ with respect to the center. As is shown in Figure 6.8, the total voltage over the plate is then V_{b} and the current through the plate is detected by comparing it to an adjustable resistance at room temperature. When the plate resistance is equal to the adjustable resistance, the output of the resistance bridge is zero. Since a DC measurement is susceptible to drifts, we alternate the voltage V_{b} at $63\,\mathrm{Hz}$ with an amplitude of $0.5\,\mathrm{V}$. The bridge imbalance output can then be monitored with a lock-in amplifier.

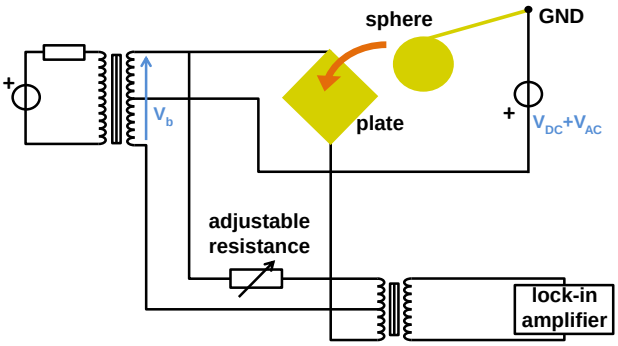

Figure 6.8: Schematic of the implementation of an extra plate resistance measurement while keeping the center of the plate at the desired potential for the electrostatic calibration.

At room temperature, we set the reference resistance to be equal to the plate's resistance. During cool-down we monitor the bridge output and the temperature of the plate. At the superconducting transition of the plate we observe a sudden jump in the bridge output, as shown in Figure 6.9. This jump is visible every time we heat or cool the plate through the superconducting transition. Since this detection method does not interfere with our other voltages, we can apply it during a Casimir measurement run and tell for each data point whether the plate was superconducting or not.

A real-time monitoring of the plate's resistance is necessary, since the critical temperature depends not only on the parameters of the NbTiN coating, but also on set-up parameters that may differ per measurement run. This is demonstrated in Fig-

ure 6.9. Using a heater in the cryostat, we have swept the temperature of the plate through its superconducting transition as measured by the bridge imbalance output. During this sweep we have switched off the lasers and all unnecessary voltages. The sphere was retracted to a distance of several millimeters. Under these conditions, we measured a critical temperature of $13.7\,\mathrm{K}$ for the NbTiN coating (see yellow dots in Figure 6.9). Next we repeated these sweeps, but now we switched the laser feeding the plate interferometer on at different laser powers.

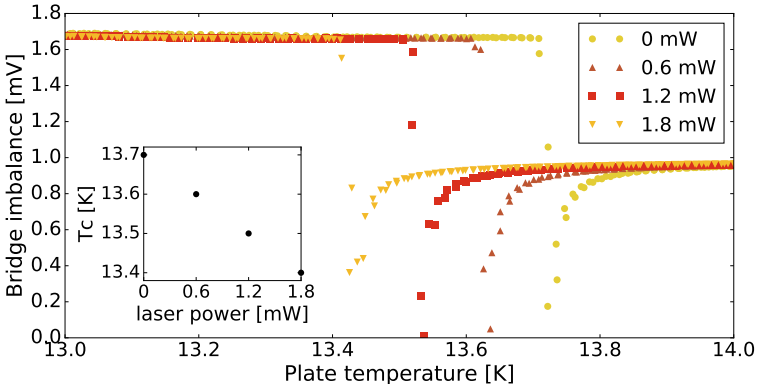

Figure 6.9: Output of the resistance bridge as a function of plate temperature. A sudden jump in the output is caused by the superconducting transition of the plate. The critical temperature of the NbTiN is found to be $13.7\,\mathrm{K}$, but depends on the power of the laser light incident on the plate. The inset shows a linear dependence of the measured transition temperature on the laser power.

It is clear from the plot that the measured transition temperature is lowered when light shines on the plate. The inset shows a linear dependence on laser power, with the critical temperature being lowered to $13.4\,\mathrm{K}$ at $1.8\,\mathrm{mW}$ laser power. At low temperature, we use a laser power of $0.4\,\mathrm{mW}$ at the plate. There are several explanations for this behaviour. Since the laser light heats the plate from above and the thermometer is placed underneath, the plate may be warmer than the thermometer monitors, such that the actual critical temperature remains unaltered. It is also likely that the light negatively influences the superconducting state, thus lowering its critical temperature [159]. More precise measurement can find the actual reason behind this phenomenon, but lie outside the scope of this thesis.